AIAA SciTech Forum
6-10 January 2025, Orlando, FL
AIAA SCITECH 2025 Forum

10.2514/6.2025-1624

Vertical Wind Velocity Estimation during UAS Fire Plume Encounters

Mosarruf H. Shawon*, Haiyang Chao†
University of Kansas, Lawrence, Kansas, 66045, USA

Matthew Rhudy‡
Pennsylvania State University, Reading, Pennsylvania, 19610, USA

Tor Arne Johansen§
Norwegian University of Science and Technology, Trondheim, N-7491, Norway

Pengzhi Tian¶, Harold P. Flanagan‖, and Jacksen Goyer**
University of Kansas, Lawrence, Kansas, 66045, USA

Wildland fires present significant challenges for aircraft emergency response operations, including firefighting, surveillance, and cargo/crew transportation. The high temperature and strong turbulence near or within fire-generated plumes can be hazardous or catastrophic for manned and unmanned aircraft. In this paper, KHawk Zephyr3, a small fixed-wing unmanned aircraft system (UAS), was sent to fly through fire-generated plumes during a prescribed grass fire to collect the UAS response data in autopilot mode. During the fire plume encounters, the unmanned aircraft experienced significant changes in acceleration, angular rate, attitude, altitude, airspeed, and ground speed. Based on the collected UAS response data, two model-aided wind velocity estimation algorithms, a 2-state extended Kalman filter (EKF) and a 9-state EKF, were developed for the calculation of vertical wind velocity along the plume encounter flight trajectory. Both simulation and flight test results showed the effectiveness of the two vertical wind estimation algorithms. Based on simulation analysis, the 2-state EKF (inertial angles of attack and sideslip) performs slightly better than the 9-state EKF for wind velocity estimation. During the two selected UAS plume encounters, the updraft velocity within the fire generated plumes is estimated to be in the range of 6-10 m/s at a height of approximately 115 meters above the ground level.

Nomenclature

IMU	=	inertial measurement unit
UAS	=	unmanned aircraft system
EKF	=	extended Kalman filter
b	=	wingspan
c	=	chord length
$C_{L_0}, C_{L_\alpha}, C_{L_q}, C_{L_{\delta_e}}$	=	components of aerodynamic lift coefficient
$C_{Y_0}, C_{Y_\beta}, C_{Y_p}, C_{Y_r}, C_{Y_{\delta_a}}, C_{Y_{\delta_r}}$	=	components of aerodynamic side force coefficient
$\overline{q}$	=	dynamic pressure
V_a	=	airspeed
α, β	=	angle of attack (AOA), angle of sideslip (AOS)

*PhD Student, Aerospace Engineering, University of Kansas, (E): mosarruf@ku.edu.
†Corresponding: Associate Professor, Aerospace Engineering, University of Kansas, (E): chaohaiyang@ku.edu.
‡Associate Professor, Division of Engineering, Business and Computing, Pennsylvania State University, Reading.
§Professor, Department of Engineering Cybernetics, Norwegian University of Science and Technology.
¶Aerospace Engineering, University of Kansas.
‖Aerospace Engineering, University of Kansas.
**Aerospace Engineering, University of Kansas.

a_x, a_y, a_z	=	x-, y-, and z-axis body accelerations
p_N, p_E, p_D	=	UAS North-East-Down position
p, q, r	=	roll, pitch, and yaw rates
u, v, w	=	x-, y-, and z-axis body velocities
W_N, W_E, W_D	=	North, East, and Down wind velocities
V_N, V_E, V_D	=	UAS North-East-Down ground speed
ϕ, θ, ψ	=	roll, pitch, and yaw angles
$\delta_e, \delta_a, \delta_r$	=	elevator, aileron, and rudder deflection
δ_t	=	throttle percentage

I. Introduction

Severe updrafts and downdrafts during wildland fires pose significant challenges for safe and efficient operations of manned and unmanned aircraft such as firefighting, surveillance, and cargo/crew transportation. Similar strong vertical air movements can be encountered by aircraft during emergencies or public good operations in convection weather, microbursts, and near complex terrains and urban canyons. Accurate measurement or estimation of the magnitude and fluctuation of these vertical flows is critical to the safe operation of the next generation of urban air mobility aircraft in these challenging environments.

Extensive research has focused on estimating two-dimensional (2D) or three-dimensional (3D) wind velocities using micro or small unmanned aircraft systems (UAS) within the aerospace engineering and meteorology communities. The 3D wind velocities along the UAS flight path can be computed directly using the wind triangulation rule after combining measurements from a multi-hole probe with a GNSS receiver and an inertial navigation system [1–3]. For instance, the 3D wind velocity vectors, including the vertical wind velocities above ocean waves, were measured using a military-grade UAS equipped with a 9-hole probe [4]. However, it is difficult and expensive to install and calibrate a multi-hole probe on small UAS due to budget, size, and maintenance limitations.

An alternative approach is to perform wind estimation utilizing low-cost micro-electromechanical systems (MEMS) sensors with stochastic filters. Various wind modeling approaches, such as the 1st and 2nd order random walk models and the sinusoidal gust model, can be used for the modeling of wind dynamics [5]. An unscented Kalman filter (UKF) was developed to estimate 3D wind velocities using UAS data from a Pitot tube, airflow mechanical vanes, and other sensors [6]. In cases when direct flow angle measurements are unavailable, model-aided estimation filters can be devised to estimate prevailing wind velocities using knowledge of aircraft dynamic models such as lift and side force coefficients [7–9]. For instance, the aerodynamic force and moments model were integrated with Extended Kalman Filter (EKF) to estimate the flow angles and 2D wind velocities without relying on an airspeed sensor in [10, 11]. Furthermore, an EKF incorporating unsteady aerodynamics has been designed and validated to reconstruct 3D prevailing wind in [12]. Similarly, longitudinal unsteady aerodynamic model-based wind estimation methods were developed and validated using flight test data over an artificial gust generator [13]. On the other hand, model-free methods utilize the sensor data only, without incorporating the aircraft's dynamic model, to produce wind estimates [14]. In summary, several wind estimation methods have been used to estimate prevailing 2D or 3D wind velocities in normal weather conditions. However, their efficacy has not been assessed in hazardous atmospheric conditions with strong updrafts or downdrafts, such as those developed within or close to wildfire plumes, volcanic plumes, or severe storms.

In the wildland fire setting, atmospheric turbulence is notably intensified, posing challenges for UAS operations. Studies indicate that when wildland fire interacts with the surrounding airflow, it may generate multiple large-scale, high-energy gusts. Moreover, wildland fires not only establish their distinct flow patterns but also amplify existing atmospheric turbulence [15]. Depending on the characteristics of the vegetation, fuels, landscape, and weather, the fire plumes are typically structured into multiple core updrafts, which are caused by the rising heat from the fire. These updrafts create zones of upward air movement, while downdrafts occur as cooler air descends. These vertical air movements profoundly impact the fire's rate of spread, intensity, and direction, ultimately shaping its behavior [16]. Strong vertical wind components can induce erratic fire behavior, including fire whirls or fire tornadoes [17].

In recent years, small UAS have become valuable tools for meteorological sensing, equipped with scientific payloads like lidar, cameras, wind anemometers, and flow sensors. They are increasingly used in fire missions for fire ignition, fire detection, and estimation of fire spread rate [18–20]. Fixed-wing UAS has also been deployed to collect volcanic plume data using various sensors, and a plume detection metric was developed using flight and atmospheric data [21]. Alternatively, a quadcopter outfitted with sonic anemometer weather stations is deployed to measure temperature, relative humidity, and wind speed at various altitudes during a prescribed wildland fire [22]. However, the high temperature and

strong turbulence in fire plumes make in-situ atmospheric sensing challenging, resulting in few experimental studies on sensing within wildland fire plumes. Simultaneous measurements of fire, smoke, and atmospheric structure are needed for understanding the fire plume dynamics, as no datasets exist that connect fire-front metrics such as rate of spread, heat release, flame intensity, and plume height to vertical wind velocities [23].

This paper focuses on model-based vertical wind velocity estimation using UAS fire plume encounter data. The contributions include: 1) measurement of small UAS responses to strong updrafts and downdrafts within fire-generated plumes while flying over a prescribed grass fire in autopilot path tracking mode, which provides great insights for the safety of future aircraft operations in challenging active wildland fire environments, 2) development, comparison, and evaluation of two model-aided algorithms for vertical wind estimation using UAS responses to wind changes, and 3) estimation of vertical wind velocities within grassfire generated plumes using a small fixed-wing UAS, which is the first time in the literature. In contrast, most wind estimation filters in the existing literature are validated under prevailing winds with slowly varying dynamics. Moreover, the two developed wind estimation filters are aided by UAS dynamic models identified earlier through the frequency domain system identification method [24]. These filters can be extended to other UAS operations in complex wind fields such as urban canyons, mountain areas, ocean surface wind, etc.

The paper's organization can be summarized as follows. In Sec. II, the problem of vertical wind velocity estimation is formulated. Two UAS dynamic model based vertical wind velocity estimation algorithms are described in detail in Sec. III. The UAS platform and the simulation evaluation of the filters are depicted in Sec. IV. Sec. V presents the flight test data acquisition during fire plume encounters, analysis of the measured UAS response, and the results of vertical wind velocity estimation. Finally, Sec. VI concludes the paper by summarizing key findings.

II. Problem Definition and Wind Estimation Basics

This section first introduces the research problem of UAS-based vertical wind velocity estimation, and then covers the basics for UAS-based wind estimation.

A. Problem Statement

This paper focuses on the problem of vertical wind velocity estimation along the flight trajectory of a fixed-wing UAS, which is equipped with a standard avionics sensing suite, including a regular Pitot tube, a GNSS receiver, and inertial sensors. The target scenarios include updraft/downdraft velocity estimation during fire plume encounters, flight close to buildings or mountains, volcano eruptions, and power plant flue gas emissions. An example trajectory for UAS fire plume encounter flight is shown in Fig. 1, where multiple updrafts can be observed within the grass fire plumes. It is worth emphasizing that a UAS can be impacted by updrafts, downdrafts, and other circulations during such flights. The impact of severe changes in updraft/downdraft velocities will show up in the UAS control inputs and responses, including measurements such as the air data (V_a, α, β), the attitude (ϕ, θ, ψ), accelerations (a_x, a_y, a_z), angular rates (p, q, r), and ground speeds (V_N, V_E, V_D). These measurements can also be used as the inputs for vertical wind velocity estimation filters. Multiple methods can be used for this problem, including the direct method for UAS with flow angle measurements [5], inertial AOA and AOS-based wind estimation, other stochastic filter (Extended Kalman Filter, Unscented Kalman Filter, Particle Filter) based wind estimation, etc.

During UAS flights, the prevailing wind, gusts, and turbulence can be treated as disturbances to the aircraft's closed-loop system, which usually aims to track a reference path while maintaining the altitude as shown in Fig. 2. Turbulent conditions may introduce fluctuations in airspeed and flow angles as the relative airflow around the UAS shifts. For example, a sudden updraft, downdraft, or rapid change in the wind direction may alter the forces and moments acting on the UAS. The wind impact may quickly show up in body accelerations (a_x, a_y, a_z), as well as in the angular rates (p, q, r). These variations will consequently change the aircraft's position and attitude. When these disturbances are big enough, they will also show up in the control inputs $(\delta_a, \delta_e, \delta_r, \delta_t)$ since the closed-loop system is trying to maintain the reference flight path and attitude. Therefore, accurate wind and turbulence information is crucial for ensuring ride quality and aviation safety.

B. Wind Estimation Basics

The 3D wind velocities along the aircraft flight trajectory can be estimated by subtracting the 3D airspeed from the 3D ground speed of the UAS [5]. It can be calculated using a combination of air triplets (V_a, α, β) from a multi-hole probe or reconstructed from airdata, inertial, and GNSS measurements. The wind estimation equation can be listed as the following [5]:

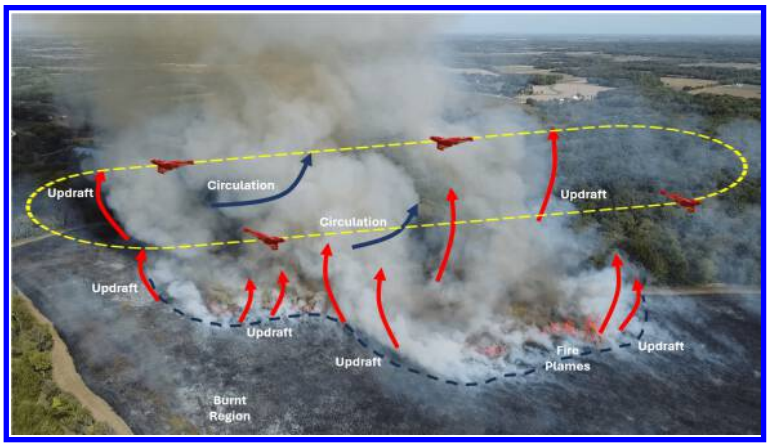

Fig. 1 Example flight trajectory for collection of UAS plume encounter datasets.

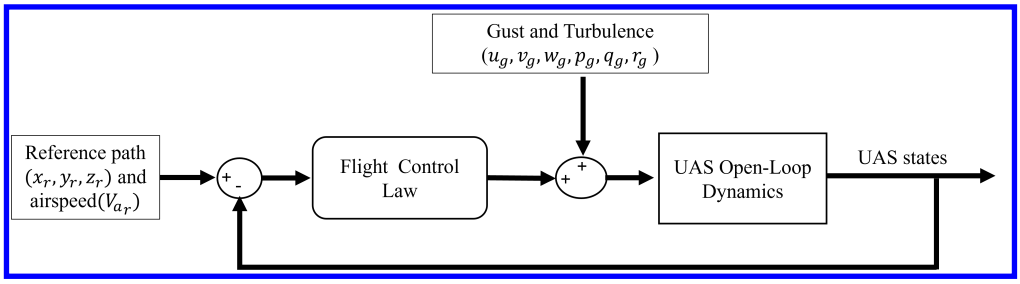

Fig. 2 Impact of wind and gust on UAS.

$$\begin{bmatrix} W_N \\ W_E \\ W_D \end{bmatrix} = \begin{bmatrix} V_N \\ V_E \\ V_D \end{bmatrix} - R_b^v(\phi, \theta, \psi) \begin{bmatrix} V_a \cos\alpha \cos\beta \\ V_a \sin\beta \\ V_a \sin\alpha \cos\beta \end{bmatrix} \tag{1}$$

where R_b^v is the rotation matrix from the aircraft body frame to the NED frame:

$$R_b^v(\phi, \theta, \psi) = \begin{bmatrix} \cos\theta\cos\psi & \sin\phi\sin\theta\cos\psi - \cos\phi\sin\psi & \cos\phi\sin\theta\cos\psi + \sin\phi\sin\psi \\ \cos\theta\sin\psi & \sin\phi\sin\theta\sin\psi + \cos\phi\cos\psi & \cos\phi\sin\theta\sin\psi - \sin\phi\cos\psi \\ -\sin\theta & \sin\phi\cos\theta & \cos\phi\cos\theta \end{bmatrix}. \tag{2}$$

This direct wind estimation method is effective when accurate direct measurements of flow angles from multi-hole probes or vanes are available and high-fidelity inertial sensors are used for orientation measurements. Vertical wind velocity can also be estimated using a setup that includes an IMU, a GNSS receiver, and a standard Pitot tube when an accurate UAS dynamic model is available, which is the focus of this paper.

III. Estimation of Vertical Wind Velocity

In this section, the vertical wind velocity estimation algorithms are explained in detail, including the airspeed scaling and correction, a 2-state EKF based on inertial angles of attack and sideslip, and a 9-state EKF based on the body airspeed vector and several other states.

A. Airspeed Scaling and Correction

The airspeed (V_a) for a UAS can be calculated based on the measurements from a dynamic pressure sensor connected to a Pitot tube, which is often installed at the nose or the wingtips of an aircraft. However, these measurements can be noisy and biased, and further scaling and corrections are often needed for later wind estimation. The airspeed

measurements can be calculated as :

$$V_a = \sqrt{K\frac{2P_d}{\rho}} \tag{3}$$

where P_d is the dynamic pressure, ρ is the air density, and K is the correction factor for calibration error and ideal gas assumption.

The air density (ρ) for each flight can be further calculated based on real-time measurements from static pressure and temperature sensors:

$$\rho = \frac{P_s}{RT} \tag{4}$$

where P_s is the static pressure and T is the air temperature. The correction factor K can be estimated using an EKF-based wind estimation algorithm [25–27], or calibrated in calm wind days using GNSS velocity measurements.

B. Inertial AOA/AOS based Vertical Wind Velocity Estimation

For UAS with a regular Pitot tube, inertial AOA and AOS can be estimated first through a model-based approach, and then vertical wind velocity can be calculated. By combining Eqs. (1) and (2), the vertical wind velocity can be calculated as

$$W_D = V_D + V_a(\sin\theta\cos\alpha\cos\beta - \sin\phi\cos\theta\sin\beta - \cos\phi\cos\theta\sin\alpha\cos\beta). \tag{5}$$

The inertial AOA (α) and AOS (β) can be estimated using a recursive complementary filter or an extended Kalman filter [7, 28, 29]. We propose to estimate the vertical wind velocities by utilizing the inertial AOA and AOS obtained from a 2-state EKF. The overall inertial AOA/AOS based vertical wind velocity estimation algorithm is summarized in Fig. 3. The vertical speed (V_D) and the attitude angles (ϕ, θ, ψ) are required to estimate the vertical wind velocity in addition to the inertial AOA and AOS.

The state x and input u of the 2-state EKF are:

$$\mathsf{x} = [\alpha \quad \beta]^T \tag{6}$$

$$\mathsf{u} = [a_x \quad a_y \quad a_z \quad p \quad q \quad r \quad \phi \quad \theta \quad V_a]^T \tag{7}$$

The state propagation equations for the EKF can be written as:

$$\dot{\alpha} = q - (p\cos\alpha + r\sin\alpha)\tan\beta + \frac{g(\cos\phi\cos\theta\cos\alpha + \sin\theta\sin\alpha) - a_x\sin\alpha + a_z\cos\alpha}{V_a\cos\beta} \tag{8}$$

$$\begin{aligned}\dot{\beta} = \frac{1}{V_a}[&-a_x\cos\alpha\sin\beta + a_y\cos\beta - a_z\sin\alpha\sin\beta + \\ &g(\sin\theta\cos\alpha\sin\beta + \cos\theta\sin\phi\cos\beta - \cos\theta\cos\phi\sin\alpha\sin\beta)] + p\sin\alpha - r\cos\alpha\end{aligned} \tag{9}$$

The measurement update equation is derived from the aircraft lift and side force equations [7]. The lift force on an aircraft can be approximated using lift coefficients and the projection of gravity and thrust.

$$L = C_L\bar{q}S \approx \left(C_{L_0} + C_{L_\alpha}\alpha + C_{L_{\delta_e}}\delta_e + C_{L_q}\frac{qc}{2V_a}\right)\bar{q}S = (m(a_x\sin\alpha - a_z\cos\alpha) - T\sin\alpha) \tag{10}$$

Since the thrust projection is much smaller than the lift during normal flight conditions, it can be removed for simplification. Similarly, the update equation for the angle of sideslip (β) can be derived by approximating the side force equation.

$$Y = C_Y\bar{q}S \approx \left(C_{Y_0} + C_{Y_\beta}\beta + C_{Y_p}\frac{pb}{2V_a} + C_{Y_r}\frac{rb}{2V_a} + C_{Y_{\delta_a}}\delta_a + C_{Y_{\delta_r}}\delta_r\right)\bar{q}S \approx ma_y \tag{11}$$

Then, the nonlinear measurement function (h) and the measurement vector (z) are:

$$\mathsf{h}(\mathsf{x},\mathsf{u},0) = \begin{bmatrix} \frac{m(a_x\sin\alpha - a_z\cos\alpha)}{\bar{q}S} - C_{L_\alpha}\alpha \\ \beta \end{bmatrix} \tag{12}$$

$$\mathsf{z} = \mathsf{h}(\mathsf{x},\mathsf{u},\mathsf{v}) = \begin{bmatrix} C_{L_0} + C_{L_q}\frac{qc}{2V_a} + C_{L_{\delta_e}}\delta_e \\ \frac{1}{C_{Y_\beta}}\left(\frac{ma_y}{\bar{q}S} - C_{Y_0} - \frac{C_{Y_p}p_b}{2V_a} - \frac{C_{Y_r}r_b}{2V_a} - C_{Y_{\delta_a}}\delta_a - C_{Y_{\delta_r}}\delta_r\right) \end{bmatrix} \tag{13}$$

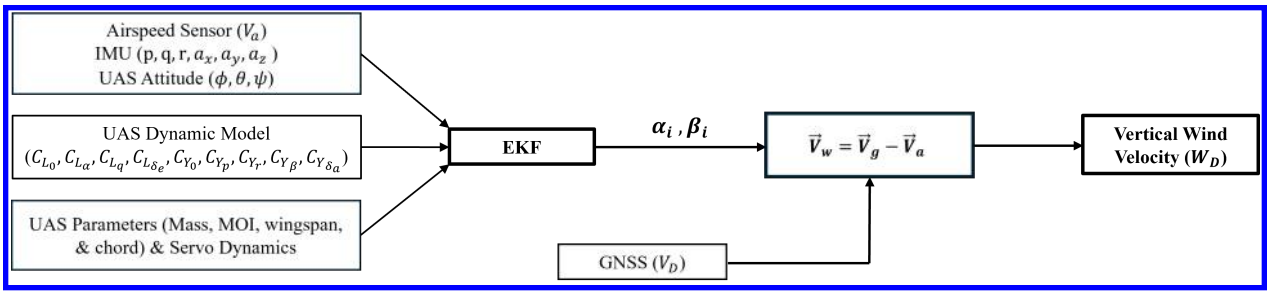

Fig. 3 The system diagram for inertial AOA & AOS-based vertical wind velocity estimation.

C. 9-state EKF-based Vertical Wind Velocity Estimation

As an alternative, a 9-state EKF can be used to estimate the vertical wind velocity together with other system states using similar UAS dynamics equations [9]. It can simultaneously estimate the body-axis velocity components (u, v, w), attitude (ϕ, θ, ψ), and wind velocity components (W_N, W_E, W_D).

This filter uses the GNSS ground velocities (V_N, V_E, V_D), body acceleration (a_x, a_y, a_z), angular rates (p, q, r), and airspeed (V_a) measurements as the filter inputs. It also uses UAS stability and control derivatives, including the lift coefficients (C_L), side force coefficients (C_Y), and UAS control surface deflections (δ_a, δ_e, δ_t). The state x and input u of the 9-state EKF are:

$$\mathsf{x} = [u \quad v \quad w \quad \phi \quad \theta \quad \psi \quad W_N \quad W_E \quad W_D]^T \tag{14}$$

$$\mathsf{u} = [a_x \quad a_y \quad a_z \quad p \quad q \quad r]^T \tag{15}$$

The propagation equations (Eqs. (16-19)) are based on the translational and rotational motion of the aircraft, and the measurement equations (Eqs. 20 and 21) are based on the combination of the wind triangle equation, air triplets calculation, and aircraft lift and side force equations. The air triplets $[V_a, \alpha, \beta]$ are expressed as aircraft body-axis velocity components $[u, v, w]$. The wind dynamics are modeled as the random walk process such that wind acceleration $[\dot{W}_N, \dot{W}_E, \dot{W}_D]^T$ is equal to zero mean Gaussian noise [9]. This random walk model has been shown to work for the prevailing wind estimation, where the wind acceleration is typically assumed to be slow-varying. Consequently, the wind acceleration terms in the velocity derivatives (Eq. (17)) can be neglected under the assumption of slow-evolving wind dynamics. These assumptions might affect the filter performance in fast-changing complex wind field conditions such as fire plumes, which will be discussed in later simulation and flight test results.

$$\dot{\mathsf{x}} = \begin{bmatrix} \dot{u} & \dot{v} & \dot{w} & \dot{\phi} & \dot{\theta} & \dot{\psi} & \dot{W}_N & \dot{W}_E & \dot{W}_D \end{bmatrix}^T \tag{16}$$

$$\begin{bmatrix} \dot{u} \\ \dot{v} \\ \dot{w} \end{bmatrix} = \begin{bmatrix} rv - qw \\ pw - ru \\ qu - pv \end{bmatrix} + \begin{bmatrix} a_x \\ a_y \\ a_z \end{bmatrix} + \begin{bmatrix} -g \sin\theta \\ g \cos\theta \sin\phi \\ g \cos\theta \cos\phi \end{bmatrix} + R_v^b(\phi, \theta, \psi) \begin{bmatrix} \dot{W}_N \\ \dot{W}_E \\ \dot{W}_D \end{bmatrix} \tag{17}$$

$$\begin{bmatrix} \dot{\phi} \\ \dot{\theta} \\ \dot{\psi} \end{bmatrix} = \begin{bmatrix} 1 & \sin\phi \tan\theta & \cos\phi \tan\theta \\ 0 & \cos\phi & -\sin\phi \\ 0 & \sin\phi/\cos\theta & \cos\phi/\cos\theta \end{bmatrix} \begin{bmatrix} p \\ q \\ r \end{bmatrix} \tag{18}$$

$$\begin{bmatrix} \dot{W}_N \\ \dot{W}_E \\ \dot{W}_D \end{bmatrix} = \begin{bmatrix} 0 \\ 0 \\ 0 \end{bmatrix} + W_{w_k} \tag{19}$$

where W_{w_k} is zero mean white Gaussian noise.

Then, the nonlinear measurement function h and the measurement z vector are:

$$\mathsf{h}(\mathsf{x},\mathsf{u},0)=\begin{bmatrix} u\cos\psi\cos\theta+v(-\sin\psi\cos\phi+\cos\psi\sin\theta\sin\phi)+w(\sin\psi\sin\phi+\cos\psi\sin\theta\cos\phi)+W_N \\ u\sin\psi\cos\theta+v(\cos\psi\cos\phi+\sin\psi\sin\theta\sin\phi)+w(-\cos\psi\sin\phi+\sin\psi\sin\theta\cos\phi)+W_E \\ -u\sin\theta+v\cos\theta\sin\phi+w\cos\theta\cos\phi+W_D \\ u \\ \frac{m(a_x\frac{w}{\sqrt{u^2+w^2}}-a_z\frac{u}{\sqrt{u^2+w^2}})-T\frac{w}{\sqrt{u^2+w^2}}}{\frac{\rho(u^2+v^2+w^2)S}{2}}-C_{L_\alpha}\tan^{-1}(\frac{w}{u}) \\ \sin^{-1}(\frac{v}{\sqrt{u^2+v^2+w^2}}) \end{bmatrix} \tag{20}$$

$$\mathsf{z}=\mathsf{h}(\mathsf{x},\mathsf{u},\mathsf{v})=\begin{bmatrix} V_N \\ V_E \\ V_D \\ V_a \\ C_{L_o}+C_{L_{\delta_e}}\delta_e+\frac{C_{L_q}qc}{2V_a} \\ \frac{\frac{ma_y}{\bar{q}S}-C_{Y_0}-\frac{C_{Y_p}pb}{2V_a}-\frac{C_{Y_r}rb}{2V_a}-C_{Y_{\delta_a}}\delta_a}{C_{Y_\beta}} \end{bmatrix}. \tag{21}$$

D. EKF Process

This paper applies the EKF methodology detailed in [30]. The nonlinear discrete state space model (Eqs. (16 - 21)) can be written as:

$$\mathsf{x}_k=\mathsf{f}(\mathsf{x}_{k-1},\mathsf{u}_{k-1},\mathsf{w}_{k-1}) \tag{22}$$

$$\mathsf{z}_k=\mathsf{h}(\mathsf{x}_k,\mathsf{u}_k,\mathsf{v}_k) \tag{23}$$

where f is the nonlinear state function and $\mathsf{w_k}$ and $\mathsf{v_k}$ represents the process and measurement noise.

The EKF time update equations are given as

$$\hat{\mathsf{x}}_k^-=\mathsf{f}(\hat{\mathsf{x}}_{k-1},\mathsf{u}_{k-1},0) \tag{24}$$

$$P_k^-=A_kP_{k-1}A_k^T+W_kQ_{k-1}W_k^T \tag{25}$$

and the EKF measurement update equations are:

$$K_k=P_k^-H_k^T(H_kP_k^-H_k^T+R_k)^{-1} \tag{26}$$

$$\hat{\mathsf{x}}_k=\hat{\mathsf{x}}_k^-+K_k(\mathsf{z}_k-\mathsf{h}(\hat{\mathsf{x}}_k^-,\mathsf{u}_k,0)) \tag{27}$$

$$P_k=(I-K_kH_k)P_k^-. \tag{28}$$

A, W, and H are Jacobian matrices that can be calculated by

$$A_{[i,j]}=\frac{\partial\mathsf{f}[i]}{\partial\mathsf{x}[j]}(\hat{\mathsf{x}}_{k-1},\mathsf{u}_{k-1},0) \tag{29}$$

$$W_{[i,j]}=\frac{\partial\mathsf{f}[i]}{\partial\mathsf{w}[j]}(\hat{\mathsf{x}}_{k-1},\mathsf{u}_{k-1},0) \tag{30}$$

$$H_{[i,j]}=\frac{\partial\mathsf{h}[i]}{\partial\mathsf{x}[j]}(\hat{\mathsf{x}}_k^-,\mathsf{u}_k,0). \tag{31}$$

The EKF tuning process and the selection of initial covariance matrix P_0, process noise covariance matrix Q, and measurement noise covariance matrix R are discussed in Sec. V.C.2.

IV. UAS Platform and Simulation Evaluation

This section describes the UAS platform, its onboard avionics, the MATLAB-based simulation environment, and simulation results for testing and verification of the vertical wind velocity estimation algorithms.

A. UAS Platform

KHawk Zephyr3 UAS, shown in Fig. 4, was used as the experimental platform. It was developed in the Cooperative Unmanned Systems Laboratory (CUSL) at the University of Kansas [24, 31]. It was built from the RiteWing RC Zephyr3 kit [32]. The aircraft has two elevon servos for roll and pitch control and a pusher-type propeller driven by an electric brushless motor for throttle control. The total takeoff weight is around 2.2 kg. Three 11.1V 2000 mAh batteries supply the power, allowing up to 30 minutes of flight time. The detailed specifications are provided in Table 1. The KHawk Zephyr3 UAS utilizes a Pixhawk 2.4.8 autopilot running Arduplane firmware for inertial sensing, communication, flight control, and data logging. Other onboard avionics include a Ublox-Lea 6h GNSS receiver, a Pitot tube with an MPXV7002DP airspeed sensor, and two PeauPro82 GoPro Hero 4 Black cameras. The sensor update rate is 5 Hz for the GNSS receiver and 50 Hz for the airspeed sensor, inertial measurements, and the aileron/elevator control inputs. The pulse width modulation (PWM) signals from the Pixhawk to the actuator servos are recorded and processed postflight for the calculation of surface deflection angles.

Table 1 KHawk Zephyr3 UAS specifications.

UAS Specifications	KHawk Zephyr3
Mass	2.2 kg
Wingspan	1.22 m
Wing area	0.41 m^2
Mean Aerodynamic Chord	0.31 m
Cruise Speed	15 – 17 m/s

Fig. 4 KHawk Zephyr3 UAS.

B. Simulation Results

A MATLAB-based 6-DOF nonlinear simulator for the KHawk Zephyr3 UAS was developed to model the UAS's response to wind [1]. The simulator utilizes the dimensionless stability and control derivatives identified using the KHawk Zephyr3-R UAS flight test after minor adjustments [24]. Note that KHawk Zephyr3 and Zephyr3-R UAS were built using the same wing kit (RiteWing RC Zephyr3), actuator servos, throttle motors, and batteries. The autopilot board and the radio modem are different, which resulted in a slightly different inertial matrix. The elevons are slightly different, but no significant changes in the model parameters are observed from the doublet response flight data of Zephyr3, shown in Fig. 5. Theil's Inequality Coefficient (TIC) is used to evaluate the overall fit. TIC values range from 0 to 1, where 0 represents a perfect fit. The TIC for the longitudinal fit is 0.1, and the lateral dynamics is 0.24. A standard guideline is that a TIC below 0.30 signifies an accurate fit [24]. The lift/side force coefficients used are shown in Table 2. Additionally, a Proportional Integral Derivative (PID) based inner loop controller (roll and pitch hold) was designed to emulate the onboard flight controller, with the controller gains tuned using step response flight test data.

Table 2 Selected lift and side force coefficients of Zephyr3 UAS.

C_{L_0}	C_{L_α}	C_{L_q}	$C_{L_{\delta_e}}$	C_{Y_0}	C_{Y_β}	C_{Y_p}	C_{Y_r}	$C_{Y_{\delta_a}}$
0.0993	3.8652	-0.0611	0.6640	0	-0.4063	0.2112	0.5675	0

To replicate wind conditions during plume encounter flights, a combination of 3D prevailing winds, a one-minus-cosine vertical gust model, and the Dryden wind turbulence model (u_g, v_g, w_g) is used in the simulator. The average north, east, and down prevailing wind components are set to be 3 m/s, 1 m/s, and 0 m/s, respectively, along with the Dryden wind turbulence (low altitude model). A one-minus-cosine vertical gust model (w_s) is used with a gust length of 8 seconds and a magnitude of 5 m/s to simulate the strong updraft within fire-generated plumes, in addition to the prevailing wind and Dryden turbulence.

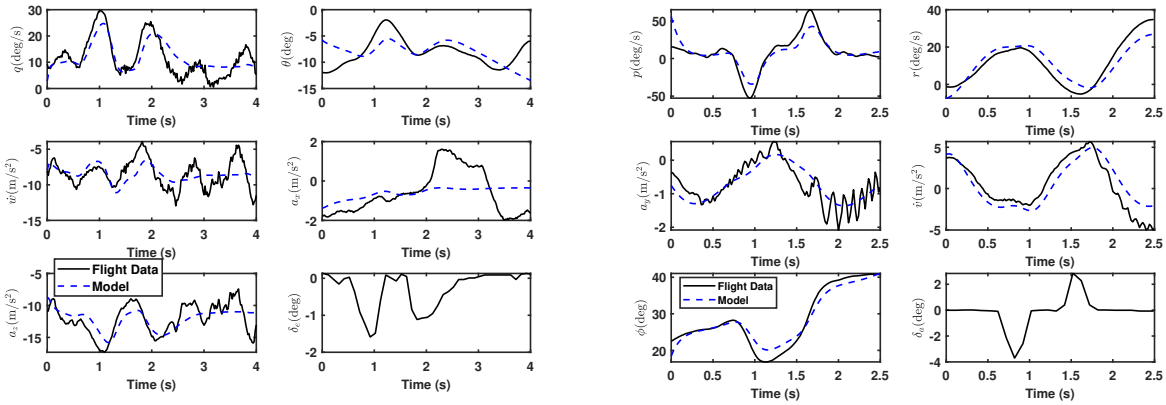

(a) Longitudinal dynamic model. **(b) Lateral dynamic model.**

Fig. 5 Comparison of the KHawk Zephyr3 UAS dynamic model with flight test data.

$$W_N = 3 + u_g \qquad W_E = 1 + v_g \qquad W_D = 0 + w_s + w_g. \tag{32}$$

The UAS was commanded to maintain a steady-state straight-level flight (zero roll angle and trim pitch angle). The airspeed was set at 20 m/s to ensure consistent flight conditions. The thrust was considered to remain constant during the simulation. The UAS's response to the wind and gust is depicted in Fig. 6.

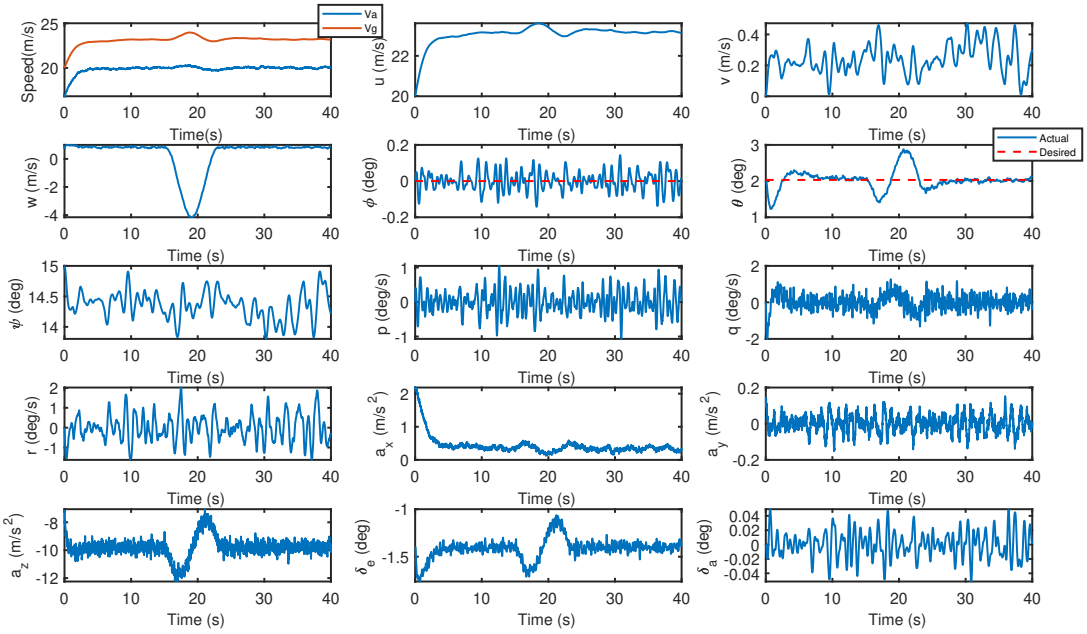

Fig. 6 UAS responses to the simulated wind field within fire plumes.

The inertial angle of attack (α) and angle of sideslip (β) are estimated using the 2-state EKF described in Sec. III.B, as illustrated in Fig. 7a. The 3D wind velocity was then estimated using Eq. (1), and the results are shown in Fig. 7b. The tuning of the process noise matrix and measurement noise matrix for both filters are kept as the same for simulation and flight test results as described in detail in Sec. V.C.2. This method demonstrated accurate estimation of the inertial

AOA and AOS, as well as the 3D prevailing wind. The RMS error for the inertial AOA and AOS are less than 0.2 deg, as summarized in Table 3. The estimated angle of attack (α) exhibited higher frequency variations compared to the true values, reflected in the estimated W_N. The RMS error for the vertical wind velocity is less than 0.1 m/s, proving the efficacy of the filter in simulation.

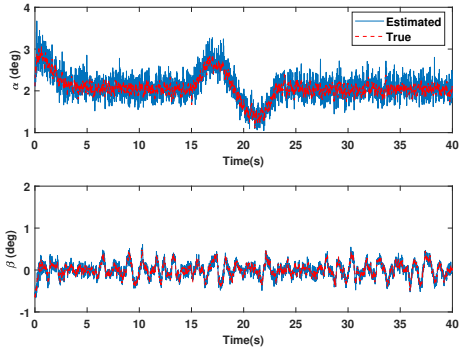

(a) Estimated inertial AOA and AOS.

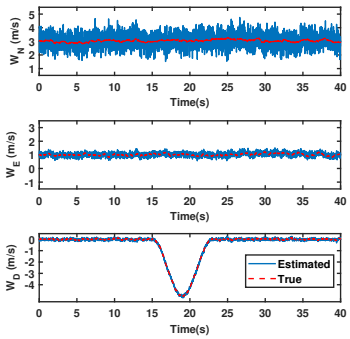

(b) Estimated 3D prevailing wind.

Fig. 7 Comparison of estimated inertial AOA, AOS, and 3D prevailing wind using the 2-state EKF.

Similarly, the 9-state EKF was used to estimate the 3D wind velocity, the body airspeed components, and the UAS attitude, as detailed in Section III.B. The RMS errors, excluding the convergence phase for the inertial AOA and AOS and 3D wind estimates, are summarized in Table 3. It can be observed that the performance of the 2-state EKF-based wind estimation is slightly better than that of the 9-state EKF. This is partially due to the estimation error for pitch and yaw angles (about 2 degrees). In addition, the estimated yaw angle has a constant bias which is reflected in the estimation error of W_E. One possible reason is that the wind velocity is assumed to be a random walk in the 9-state EKF, which is applicable under steady atmospheric wind conditions. Besides, introducing discrete gusts adds nontrivial wind acceleration to the system, which may contribute to the performance degradation of this EKF in specific scenarios. The inaccuracies in wind modeling and attitude estimation affect state estimates due to the coupling between states.

Table 3 Estimation errors.

	RMSE α	RMSE β	RMSE W_N	RMSE W_E	RMSE W_D
2 State EKF	0.1761 deg.	0.0646 deg.	0.4934 m/s	0.1312 m/s	0.0603 m/s
9 State EKF	0.1109 deg.	0.1023 deg.	0.38 m/s	1.755 m/s	0.9427 m/s

V. UAS Plume Encounter Flight Test and Wind Estimation Results

This section describes the UAS plume encounter flight test, the data set, and the vertical wind estimation results using two discussed methods: 1) the 2-state EKF (inertial AOA and AOS) based method and 2) the 9-state EKF-based method.

A. Plume Encounter Data Acquisition

A flight test was conducted from 12:51 pm to 1:01 pm (Central Day Time) on April 08, 2019, during a prescribed grassfire at the Baldwin Woods Preserve, Kansas, to collect the UAS fire plume encounter data. The temperature at 12:52 pm was 23 degrees Celsius, the relative humidity was 34%, and the ambient wind during the take-off was approximately 2.57 m/s from the south (200 deg), according to the closest airport weather station (KANSAS ASOS at Lawrence) [33]. The prescribed burn area was approximately 440 m long and 190 m wide. During the burn, the KHawk Zephyr3 UAS was deployed to measure fire perimeter and wind velocities simultaneously [31]. The UAS was flown in automatic mode to track a desired altitude of 115 m above ground level at a cruise airspeed of 17.5 m/s. During the experiment, the UAS followed a racing car pattern consisting of two straight stretches and two semi-circular arcs.

The UAS was flown into the fire plumes during the straight portions for safety considerations. The flight trajectory, including the locations where the fire plume was encountered, is illustrated in Fig. 8. A ground image of the fire plume and a UAS aerial photo taken within fire generated plumes are shown in Fig. 9, where strong updrafts, downdrafts, and circulations can be observed.

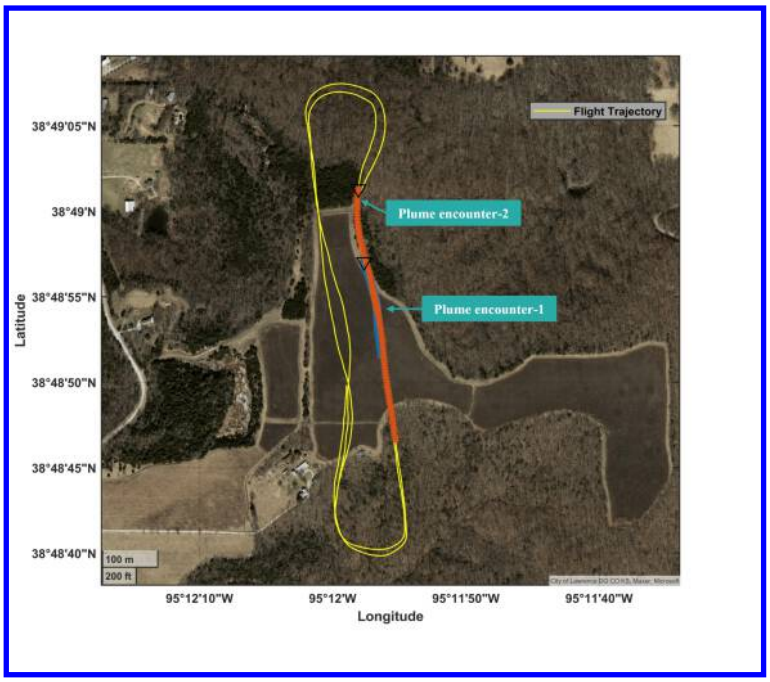

Fig. 8 Trajectory of KHawk Zephyr3 UAS during plume encounter flight test.

B. UAS Response during Fire Plume Encounter

During the flight test, the UAS flew into the fire plumes multiple times. Two UAS fire plume encounters with significant state deviation from steady state flight were identified (V_a, a_x, a_z, q, and θ). The 3D UAS flight trajectories during the fire plume encounters are depicted in Fig. 10, where the blue triangle shows the start point. During the plume encounters, the UAS altitude changed by more than ±10 m within a 10-second period, although the desired altitude was kept at 115 m. The measured UAS responses during two fire plume encounters are shown in Figs. 11 and 12. It can be observed from Fig. 11 that the UAS encountered the fire plume at around 399 s, which is marked by a surge in airspeed (V_a) from 17.8 to 22.5 m/s. Simultaneously, the body z acceleration (a_z) increased from -9.4 to -22.7 m/s^2 (2g up acceleration) and body x acceleration (a_x) rose by 2.2 m/s^2. The angular rates also changed significantly, with the pitch rate reaching to 25 deg/s within 2 seconds and the roll rate increasing to 60 deg/s. During this plume encounter, the throttle remained about the same, and the elevators and ailerons changed more than 1.5 degrees from the trim values. The first plume encounter lasted for about 5 seconds (399 - 404 s). Upon exiting the plume, fluctuations in these parameters decrease notably.

Similar UAS responses can be noticed from the second plume encounter data shown in Fig. 12. A comparable trend can be identified in the body z acceleration (a_z), body x acceleration (a_x), and pitch rate (q). The UAS remains within the fire plume for 15 seconds (485 - 500 s). During this encounter, the longitudinal states (V_a, a_x, a_z, q, and θ) fluctuated rapidly, and the airspeed (V_a) changed by 6.5 m/s. Notable tracking errors are observed between the desired and actual attitude angles during both plume encounters. Note that the change in pitch rate preceded the elevator deflections in both plume encounters, suggesting that the inner loop controller is attempting to counter-react to the fire-generated updrafts/downdrafts.

(a) Ground photo. **(b) Aerial photo captured by the onboard RGB camera.**

Fig. 9 Ground and aerial photos of UAS flying through fire generated plumes.

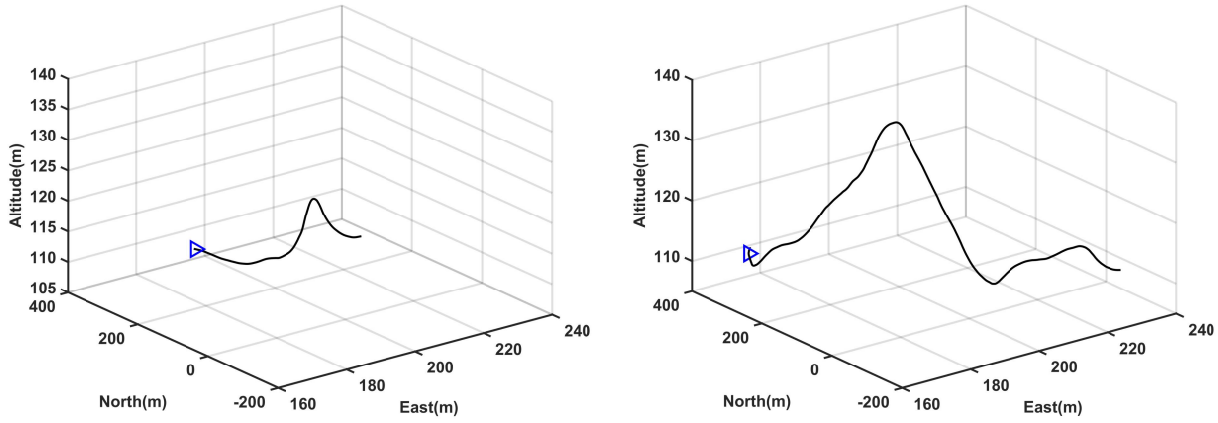

(a) Encounter 1 (396 - 406 s). **(b) Encounter 2 (483 - 508 s).**

Fig. 10 3D UAS flight trajectory during fire plume encounters.

C. Wind Estimation Results

1. Preprocessing of Airspeed Measurements

The airspeed measurements were preprocessed before being fed to the two wind estimation algorithms. The correction factor K in Eq. (3) was estimated using an EKF [25]. It was determined using ground weather station wind measurements from a Campbell Scientific CSAT3b 3D wind sonic anemometer (RMSE < 0.3 m/s), which were corrected for altitude using the wind profile power law. Additionally, the calculated correction factor was checked using four other flight data sets on different days, which had varying atmospheric temperature and static pressure values. The airspeed measurements are also filtered using a 4 Hz Butterworth filter. The corrected airspeed, raw airspeed measurements, and the GNSS ground velocity of the plume encounter flight are shown in Fig. 13.

2. Tuning of the EKF

Tuning of the noise covariance matrices of an EKF can be a complex and time-consuming process due to the involvement of multiple states and inputs. In this paper, the IMU measurement noise covariance matrices (σ_{a_x}, σ_{a_y}, σ_{a_z}, σ_p, σ_q, σ_r, σ_ϕ, σ_θ) were computed through ground testing and other covariances were tuned manually. In the 9-state EKF, the ability to estimate wind variation is dictated by the magnitude of the white noise in the random walk model, which can be treated as the cutoff frequency of the wind variations that can be effectively captured [26]. The noise covariance matrices (σ_α, σ_β, σ_{V_N}, σ_{V_E}, σ_{V_D}, σ_{W_N}, σ_{W_E}, σ_{W_D}, σ_{Z_5}, σ_{Z_6}) were tuned by comparing the estimated wind velocity with measurements from CSAT3b 3D wind sonic anemometer using another UAS flight data set. The tuning flight test was conducted on a separate day, with the mean prevailing wind of W_N = 4.5 m/s, W_E = 1.6 m/s, and W_D = 0.5 m/s, based on the same ground wind anemometer. To ensure accuracy, the wind speed measured by the ground weather

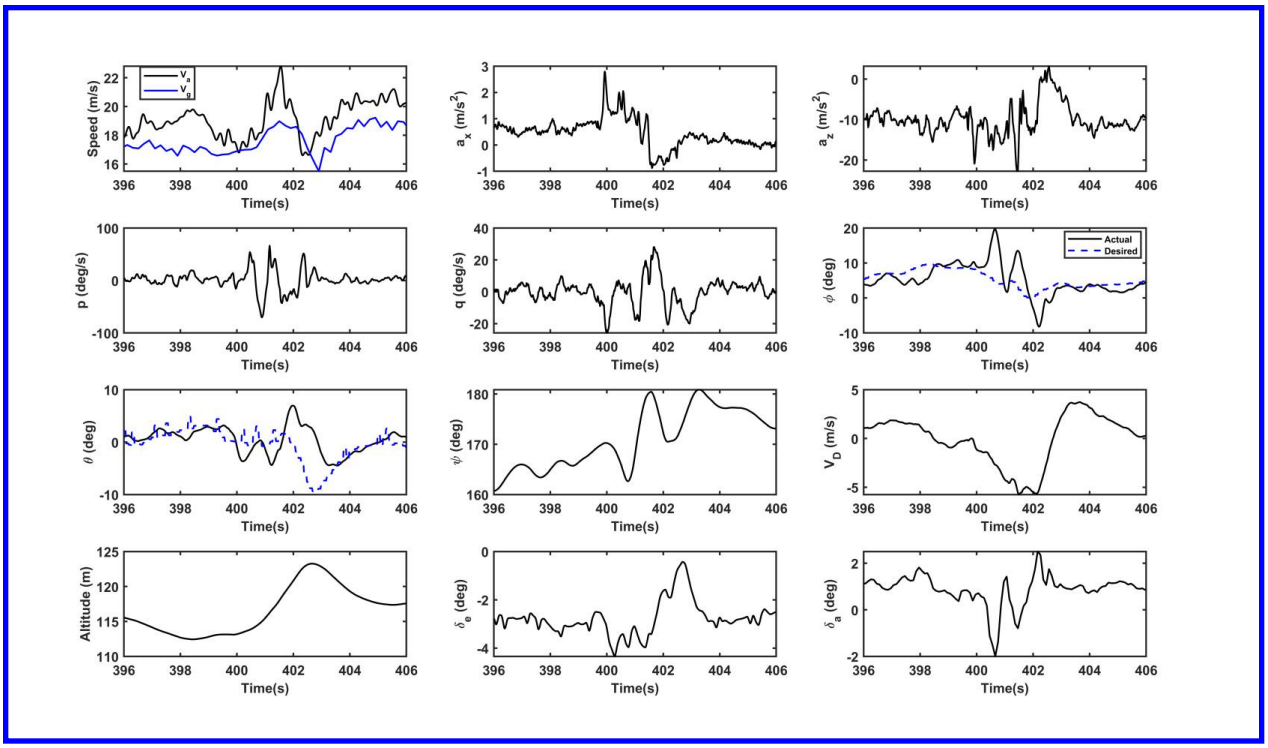

Fig. 11 UAS responses during fire plume encounter 1 (396 - 406 s).

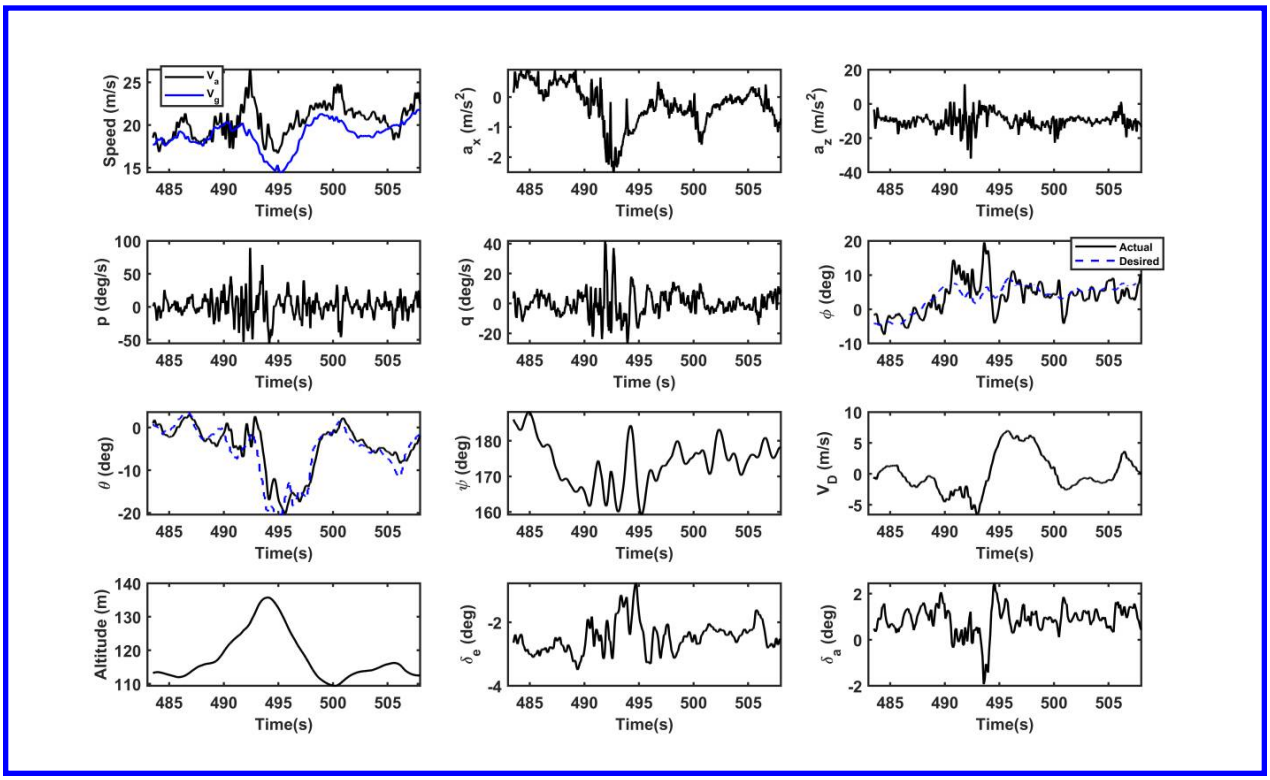

Fig. 12 UAS responses during fire plume encounter 2 (483 - 508 s).

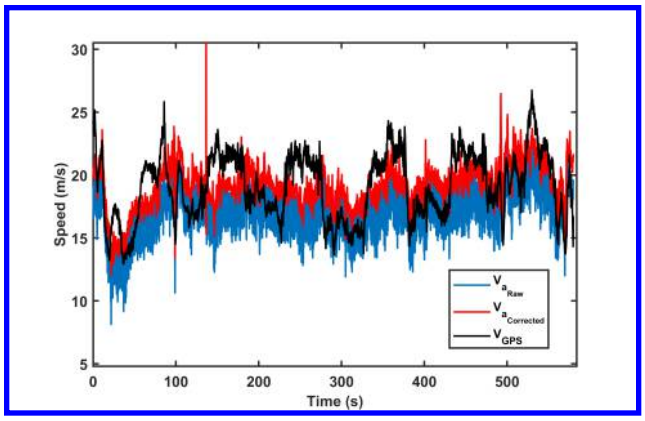

Fig. 13 Airspeed correction and scaling.

station was corrected for altitude using the wind profile power law [5]. The tuning objective is to minimize the RMS error between the estimated wind velocities and the corrected weather station measurement. This approach significantly reduces the overall tuning effort. The selected process and measurement noise matrices for both the 2-state EKF and the 9-state EKF are provided in Table 4. It is important to note that the process noise covariance matrix (Q) and the measurement noise covariance matrix (R) were both assumed to only have nonzero diagonal components. Additionally, the initial state covariance P_0, representing the state vector x, was set as an identity matrix in this paper as a general case.

Table 4 Selected 2-State and 9-State EKF tuning parameters.

2-State EKF		**9-State EKF**	
Process noise Q		**Process noise Q**	
$\sigma^2_{a_x}$	0.0089^2 (m/s^2)^2	$\sigma^2_{a_x}$	0.0089^2 (m/s^2)^2
$\sigma^2_{a_y}$	0.0089^2 (m/s^2)^2	$\sigma^2_{a_y}$	0.0089^2 (m/s^2)^2
$\sigma^2_{a_z}$	0.0089^2 (m/s^2)^2	$\sigma^2_{a_z}$	0.0089^2 (m/s^2)^2
σ^2_p	0.000424^2 (rad/s)^2	σ^2_p	0.000424^2 (rad/s)^2
σ^2_q	0.000443^2 (rad/s)^2	σ^2_q	0.000443^2 (rad/s)^2
σ^2_r	0.000397^2 (rad/s)^2	σ^2_r	0.000397^2 (rad/s)^2
σ^2_ϕ	0.0035 (rad)^2	$\sigma^2_{W_N}$	0.0173^2 (m/s)^2
σ^2_θ	0.0036 (rad)^2	$\sigma^2_{W_E}$	0.0173^2 (m/s)^2
		$\sigma^2_{W_D}$	0.0173^2 (m/s)^2
Measurement noise R		**Measurement noise R**	
σ^2_α	0.0000175^2 (rad)^2	$\sigma^2_{V_N}$	0.0022^2 (m/s)^2
σ^2_β	0.0000175^2 (rad)^2	$\sigma^2_{V_E}$	0.0022^2 (m/s)^2
		$\sigma^2_{V_D}$	0.0022^2 (m/s)^2
		$\sigma^2_{Z_5}$	0.000068^2 (rad)^2
		$\sigma^2_{Z_6}$	0.000068^2 (rad)^2

3. Inertial AOA/AOS based Vertical Wind Velocity Estimation

The inertial angle of attack and angle of sideslip were estimated using the 2-state EKF described in Sec. III.B, shown in Fig. 14. It can be observed that both flow angles exhibit higher-magnitude oscillations when the UAS enters the fire plume. During the first encounter (399 - 403 s), the maximum changes in AOA and AOS were 11.1 deg and

16.4 deg, respectively, primarily due to fire-induced turbulence. In contrast, the estimated inertial AOA only fluctuated between 2.2 and 2.6 deg outside the fire plume during the straight legs. In the second encounter (483 – 508 s), the UAS flew into a multicore updraft, with the first one between 485 and 495 s and the second one from 499 to 506 s. The updraft at 485 s was stronger, resulting in maximum changes of 10.1 deg in AOA and 21.6 deg in AOS.

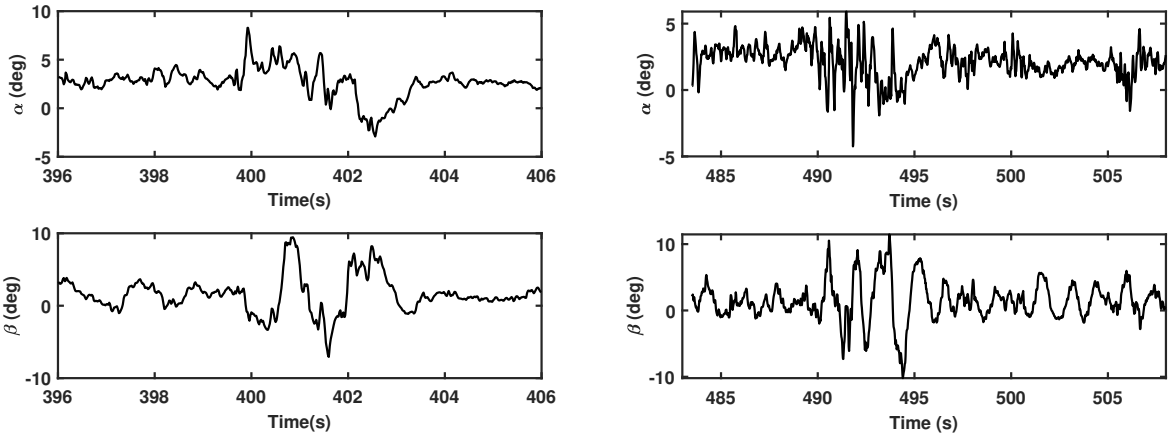

(a) Encounter 1 (396 - 406 s). **(b) Encounter 2 (483 - 508 s).**

Fig. 14 Estimated inertial AOA and AOS during fire plume encounters (2-state EKF).

Then, the estimated inertial angle of attack (α) and angle of sideslip (β) are utilized to calculate the vertical wind velocities, shown in Figs. 15 and 16. The maximum estimated vertical wind velocity reached to 8.2 m/s and 8.3 m/s for the first and second encounters, respectively. The upward wind components along the flight trajectory are shown in Figs. 15b and 16b. During the first and second fire plume encounters, the changes of vertical wind velocities are as big as 9.81 m/s and 9.66 m/s, respectively. A pattern of downdraft-updraft-downdraft can be observed for both plume encounters, which showed the strong circulation within the fire-generated plume. Additionally, the north and east wind velocity components (W_N and W_E) were also estimated, shown in Fig. 17. It can be observed that the horizontal wind magnitude and direction changed rapidly when the UAS flied inside the fire plumes. This matches with the trend from the tower weather station wind measurements during another prescribed grass fire from the literature [34]. It is worth emphasizing that it is challenging to measure the ground truth for vertical wind velocities within fire generated plumes for error quantification.

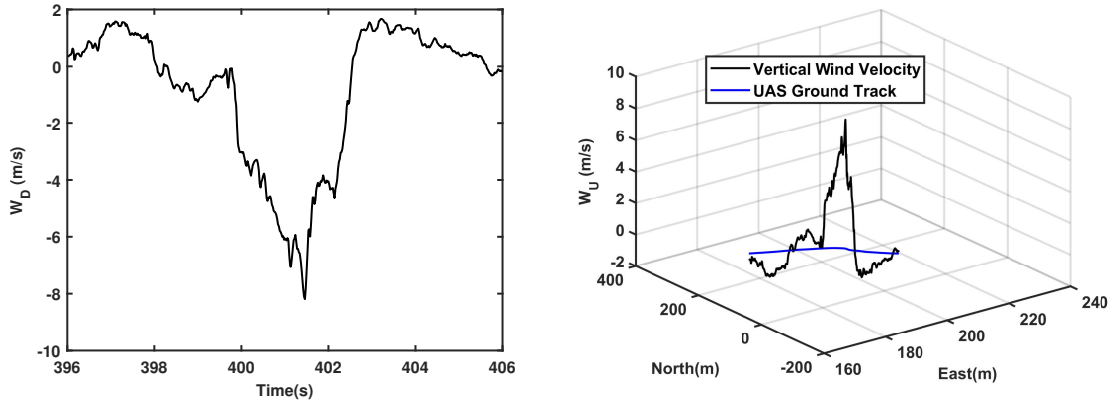

(a) Estimated vertical wind (- represents updraft). **(b) Estimated W_u along the flight trajectory (+ represents updraft).**

Fig. 15 Estimated vertical wind velocity along the flight trajectory during fire plume encounter 1 (2-state EKF).

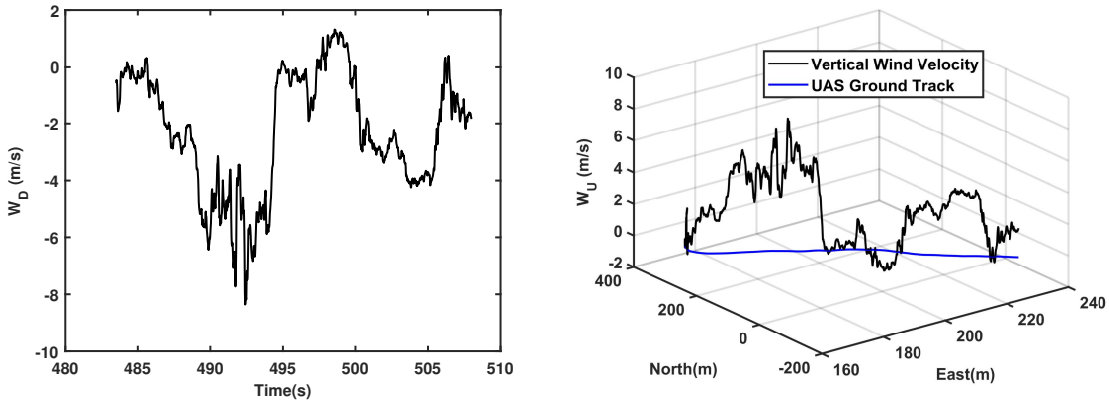

(a) Estimated vertical wind (- represents updraft).

(b) Estimated W_u along the flight trajectory (+ represents updraft).

Fig. 16 Estimated vertical wind velocity along the flight trajectory during fire plume encounter 2 (2-state EKF).

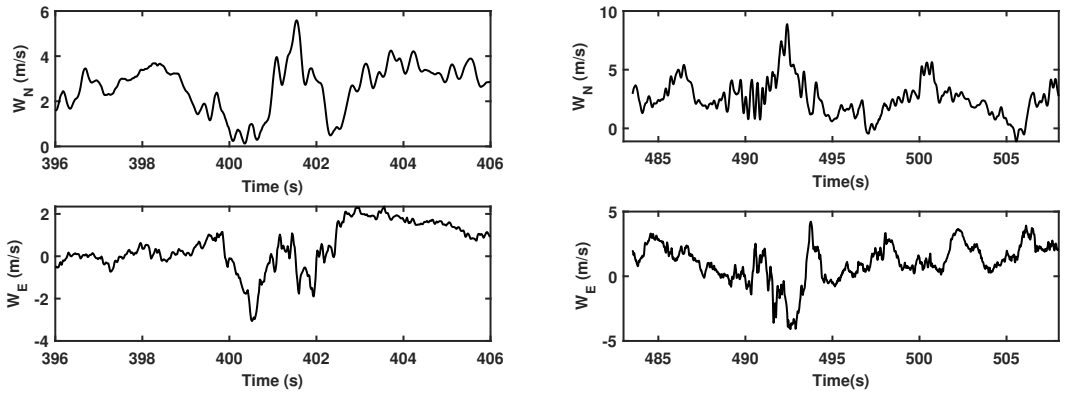

(a) Encounter 1 (396-406 s).

(b) Encounter 2 (483 - 508 s).

Fig. 17 Estimated northward and eastward wind components (2-state EKF).

4. 9-State EKF-based Vertical Wind Velocity Estimation

The 9-state EKF was further used for the estimation of the 3D wind velocity. The estimated states for both encounters are shown in Figs. 18 and 19. It can be observed that the maximum estimated vertical wind velocity reached to 4.56 m/s and 9.89 m/s during the two encounters which is slightly different than the results of the 2-state EKF. One reason causing that is the attitude estimation difference between the 9-state EKF and the Pixhawk estimates, with a bigger disagreement on the pitch angle as shown in Fig. 18. Another reason for this discrepancy is that the EKF assumes a random walk wind model throughout the flight and neglects the rotational components (p_g, q_g, r_g) of wind velocity. This assumption is reasonable under normal atmospheric conditions where the wind changes gradually. However, during fire plume encounters with strong updrafts or downdrafts, the vertical and horizontal wind velocities can change abruptly, so the random walk model may not capture the wind variations accurately. This may lead to underestimating of the vertical wind velocities and discrepancies in attitude estimation. A comparison between the estimation results for both methods is shown in Fig. 20. It can be seen that the overall trends for both methods are similar.

In summary, the maximum updraft velocity for this tallgrass prescribed fire is estimated to be in the range of 6-10 m/s at an altitude of 115 m. This value highlights the significant power generated by such wildland fires. The response of the UAS during these encounters indicates that fire plumes can induce rapid and substantial changes not only in airspeed but also in pitch rate, roll rate, and horizontal and vertical accelerations. Two wind estimation methods were evaluated using the plume encounter flight test data. The 2-state EKF-based method probably provides more accurate

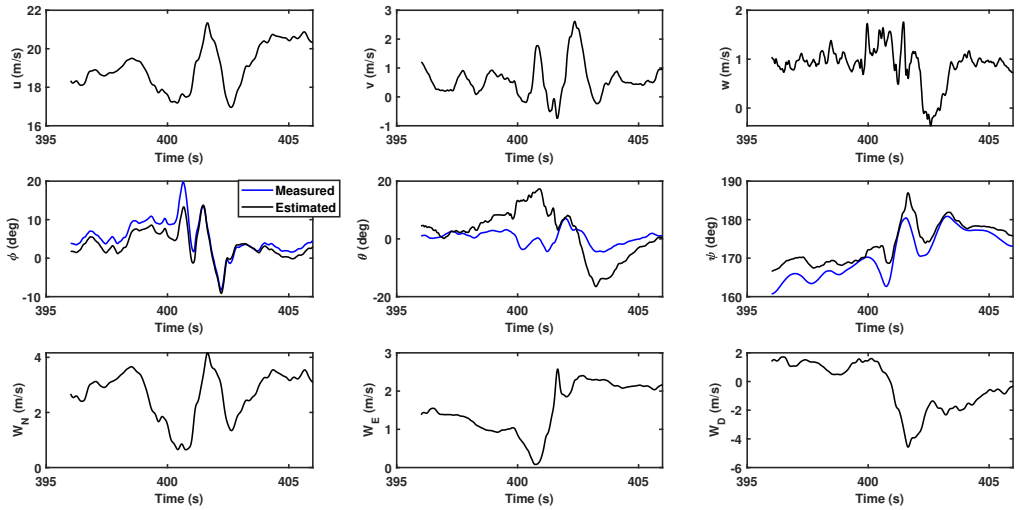

Fig. 18 Estimated airspeed components, attitude and 3D wind during encounter 1 (9-state EKF).

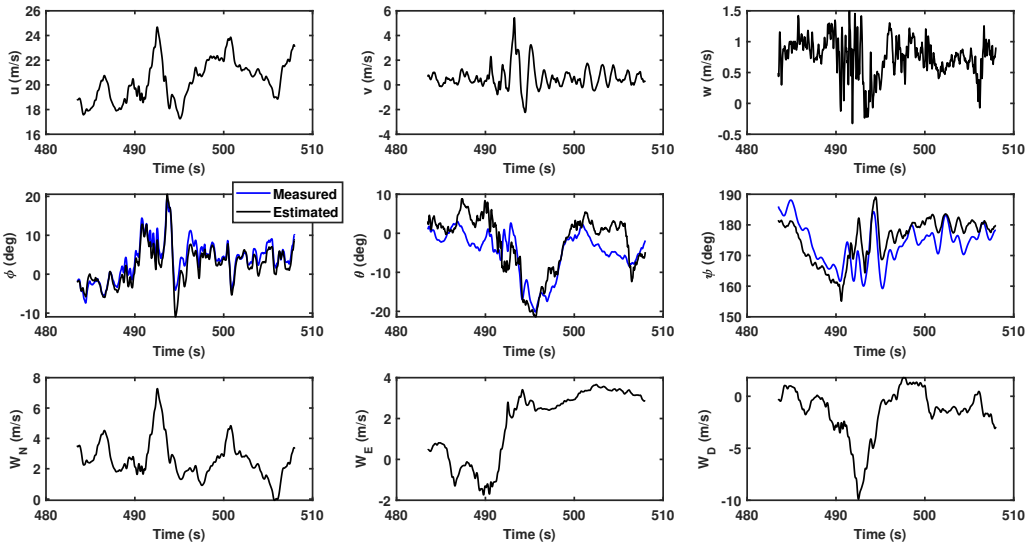

Fig. 19 Estimated airspeed components, attitude and 3D wind during encounter 2 (9-state EKF).

vertical wind velocity estimation results than the 9-state EKF-based wind estimation approaches, if the error trend is similar to simulation results.

D. Discussion and Uncertainty Analysis

Estimation inaccuracies can arise from various factors, including sensor resolution, measurement accuracy, update rate, and modeling errors. Each sensor has inherent limitations. For instance, an IMU may have bias and experience drift over time, a GNSS receiver may be affected by signal interference and outage, and a Pitot tube may be prone to calibration errors and environmental conditions. The IMU and GNSS error dynamics in the simulation environment, described in Section .IV.B, are modeled as zero-mean Gaussian noise. The simulation environment can be improved by modeling the IMU and GNSS error dynamics using stochastic models (e.g., Markov, Gauss Markov model, etc.), which

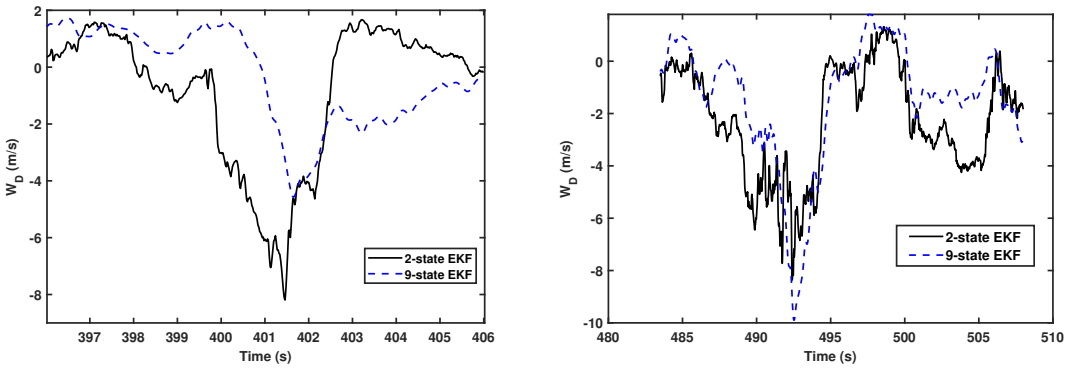

(a) Encounter 1 (396 - 406 s). **(b) Encounter 2 (483 - 508 s).**

Fig. 20 Comparison of estimated vertical wind velocities.

are more realistic to flight conditions.

Another important factor contributing to the filter efficacy is the modeling of the wind dynamics. The 9-state EKF assumes a random walk wind model and neglects gust induced rotation rates (p_g, q_g, r_g), which is reasonable under atmospheric conditions with slowly varying wind dynamics. Also, neglecting wind acceleration in the body velocity derivatives can lead to performance degradation. However, during fire plumes or discrete gust encounters, wind velocity and direction may change abruptly, limiting the model's accuracy.

Additionally, the selection of wind velocity covariance matrix during the tuning of the 9-state EKF can significantly influence the filter's accuracy, as these parameters depict the wind acceleration, with larger values indicating a higher rate of change in the wind dynamics. The tuning process can be more efficient if external wind velocity measurements such as LiDAR or SODAR are available.

To quantify the uncertainty in vertical wind velocity estimation, the Gaussian error propagation method is applied to the 2-state EKF-based vertical wind velocity estimation as it demonstrated a better performance. Assuming that the airspeed (V_a), vertical velocity (V_D), AOA (α), AOS (β), roll angle (ϕ), and pitch angle (θ) measurements/estimates are independent and follow a Gaussian distribution, the variance of the standard error of W_D can be expressed as:

$$\sigma_{W_D}^2 = \sum_{i=1}^{n} \left(\frac{\partial W_D}{\partial x_i} \sigma_{x_i} \right)^2 \tag{33}$$

where x_i represents the variables $[V_D, V_a, \alpha, \beta, \phi, \theta]$ and σ_{x_i} denotes their corresponding uncertainties.

Using the measured RMS sensor errors, estimation errors of the flow angles, and the Gaussian error propagation equation, the estimated error standard deviation of vertical wind velocity(σ_{W_D}) is ±0.4539 m/s. This estimate reflects the combined effect of all sensor uncertainties and highlights the potential limitations of the vertical wind velocities estimation method.

VI. Conclusion and Future Work

This paper presents a UAS plume encounter dataset, including accelerations, angular rates, attitude, altitude, airspeed, and ground speed, and the estimation of vertical wind velocities along the UAS flight trajectory using UAS-dynamic-model-based approaches. A KHawk Zephyr3 UAS was deployed to fly over fire plumes produced by a prescribed tallgrass burn in Kansas while in the automatic waypoint tracking mode. During the plume encounters, aggressive accelerations (20 m/s^2 change in vertical acceleration) and rotations (60 deg/s change in pitch rate) were observed. Furthermore, two model-based algorithms were developed to estimate vertical wind velocities along the flight trajectory. Based on our filters, the vertical wind velocities within the fire plumes ranged from 6 to 10 m/s at a height of about 115 meters above the ground level. The developed 2-state EKF (inertial AOA and AOS) based vertical wind velocity estimation method slightly outperforms the 9-state EKF, based on simulation studies.

Future work will include further validations of the vertical wind velocity estimation using the flight path reconstruction method, identification of the noise characteristics of the IMU and GNSS sensors, and introduction of new propagation models for the wind dynamics (Gauss Markov, plume dynamics model, etc.) generated by fire plumes (e.g., wind acceleration) to improve the filter performance.

Acknowledgments

The authors would like to thank Sheena Parsons and other members from Kansas Biological Survey for organizing the prescribed fire, Justin J. Matt for performing initial data analysis and the system identification of the Zephyr3R UAS, and Zhenghao Lin for providing the image in Fig. 1. This work was supported in part by the National Science Foundation Grants #2335568 and #2306603, the University of Kansas School of Engineering Research and Innovation Seed (RISe) funding, and the Research Council of Norway Grant #316425. This work was also sponsored in part by the U.S. Army Research Laboratory under Cooperative Agreement Number W911NF-22-2-0207. The views and conclusions contained in this document are those of the authors and should not be interpreted as representing the official policies, either expressed or implied, of the Army Research Laboratory or the U.S. Government. The U.S. Government is authorized to reproduce and distribute reprints for Government purposes, notwithstanding any copyright notation herein.

References

[1] Beard, R., and McLain, T., *Small Unmanned Aircraft: Theory and Practice*, Princeton University Press, 2012.

[2] Langelaan, J., Alley, N., and Neidhoefer, J., "Wind Field Estimation for Small Unmanned Aerial Vehicles," *Journal of Guidance, Control, and Dynamics*, Vol. 34, 2011, pp. 1016–1030.

[3] Calmer, R., Roberts, G., Preißler, J., Sanchez, K. J., Derrien, S., and O'Dowd, C. D., "Vertical Wind Velocity Measurements using a Five-hole Probe with Remotely Piloted Aircraft to Study Aerosol–Cloud Interactions," *Atmospheric Measurement Techniques*, Vol. 11, No. 5, 2018, pp. 2583–2599.

[4] Reineman, B. D., Lenain, L., and Melville, W. K., "The Use of Ship-Launched Fixed-Wing UAVs for Measuring the Marine Atmospheric Boundary Layer and Ocean Surface Processes," *Journal of Atmospheric and Oceanic Technology*, Vol. 33, 2016, pp. 2029–2052.

[5] Tian, P., Chao, H., Rhudy, M. B., Gross, J. N., and Wu, H., "Wind Sensing and Estimation Using Small Fixed-Wing Unmanned Aerial Vehicles: A Survey," *Journal of Aerospace Information Systems*, Vol. 18, No. 3, 2021, pp. 132–143.

[6] Rhudy, M. B., Gu, Y., Gross, J. N., and Chao, H., "Onboard Wind Velocity Estimation Comparison for Unmanned Aircraft Systems," *IEEE Transactions on Aerospace and Electronic Systems*, Vol. 53, No. 1, 2017, pp. 55–66.

[7] Tian, P., Chao, H., Flanagan, H. P., Hagerott, S. G., and Gu, Y., "Design and Evaluation of UAV Flow Angle Estimation Filters," *IEEE Transactions on Aerospace and Electronic Systems*, Vol. 55, No. 1, 2019, pp. 371–383.

[8] Tian, P., Chao, H., and Wu, H., "UAS-based Wind Estimation Using Sinusoidal Gust Model," *AIAA SCITECH Forum*, 2019.

[9] Tian, P., and Chao, H., "Model Aided Estimation of Angle of Attack, Sideslip Angle, and 3D Wind without Flow Angle Measurements," *AIAA Guidance, Navigation, and Control Conference*, 2018.

[10] Sharma, A., Laupré, G. F., Longobardi, P., and Skaloud, J., "Synthetic Wind Estimation for Small Fixed-Wing Drones," *Atmosphere*, Vol. 15, No. 11, 2024.

[11] Lie, F. A. P., and Gebre-Egziabher, D., "Synthetic Air Data System," *Journal of Aircraft*, Vol. 50, No. 4, 2013, pp. 1234–1249.

[12] Halefom, M. H., Hopwood, J. W., and Woolsey, C. A., "Unsteady Aerodynamics in Model-Based Wind Estimation from Fixed-Wing Aircraft Motion," *Journal of Guidance, Control, and Dynamics*, 2024, pp. 1–13.

[13] Halefom, M. H., Gresham, J. L., and Woolsey, C. A., "Wind Estimation from an Unsteady Aerodynamic Aircraft Motion Model," *AIAA SCITECH Forum*, 2022.

[14] Ahmed, Z., Halefom, M. H., and Woolsey, C., "Tutorial Review of Indirect Wind Estimation Methods Using Small Uncrewed Air Vehicles," *Journal of Aerospace Information Systems*, Vol. 21, No. 8, 2024, pp. 667–683.

[15] Desai, A., Goodrick, S. L., and Banerjee, T., "Investigating the Turbulent Dynamics of Small-scale Surface Fires," *Scientific Reports*, Vol. 12, 2022.

[16] Achtemeier, G. L., Goodrick, S. A., and Liu, Y., "Modeling Multiple-Core Updraft Plume Rise for an Aerial Ignition Prescribed Burn by Coupling Daysmoke with a Cellular Automata Fire Model," *Atmosphere*, Vol. 3, No. 3, 2012, pp. 352–376.

[17] Forthofer, J. M., and Goodrick, S. L., "Review of Vortices in Wildland Fire," *Journal of Combustion*, Vol. 2011, 2011, pp. 1–14.

[18] Casbeer, D., Beard, R., McLain, T., Li, S.-M., and Mehra, R., "Forest Fire Monitoring with Multiple Small UAVs," *American Control Conference*, 2005, pp. 3530–3535 vol. 5.

[19] Merino, L., Caballero, F., Martinez-de Dios, J. R., Maza, I., and Ollero, A., "An Unmanned Aircraft System for Automatic Forest Fire Monitoring and Measurement," *Journal of Intelligent and Robotic Systems*, Vol. 65, 2012, pp. 533–548.

[20] Gowravaram, S., Chao, H., Lin, Z., Parsons, S., Zhao, T., Xin, M., Hu, X., Tian, P., Flanagan, H. P., and Wang, G., "Prescribed Grass Fire Mapping and Rate of Spread Measurement Using NIR Images From a Small Fixed-Wing UAS," *IEEE Journal of Selected Topics in Applied Earth Observations and Remote Sensing*, Vol. 16, 2023, pp. 3519–3530.

[21] Schellenberg, B., Richardson, T., Watson, M., Greatwood, C., Clarke, R., Thomas, R. M., Wood, K., Freer, J. E., Thomas, H., Liu, E. J., Salama, F., and Chigna, G., "Remote Sensing and Identification of Volcanic Plumes using Fixed-wing UAVs over Volcán de Fuego, Guatemala," *Journal of Field Robotics*, Vol. 36, 2019, pp. 1192 – 1211.

[22] Brewer, M. J., and Clements, C. B., "Meteorological Profiling in the Fire Environment Using UAS," *Fire*, Vol. 3, No. 3, 2020.

[23] Liu, Y., Heilman, W. E., Potter, B. E., Clements, C. B., Jackson, W. A., French, N. H. F., Goodrick, S. L., Kochanski, A. K., Larkin, N. K., Lahm, P. W., Brown, T. J., Schwarz, J. P., Strachan, S. M., and Zhao, F., *Smoke Plume Dynamics*, Springer International Publishing, 2022, pp. 83–119.

[24] Matt, J. J., Hagerott, S. G., Svoboda, B. C., Chao, H., and Flanagan, H. P., "Frequency Domain System Identification of a Small Flying-Wing UAS," *AIAA SCITECH Forum*, 2022.

[25] Cho, A., Kim, J., Lee, S., and Kee, C., "Wind Estimation and Airspeed Calibration using a UAV with a Single-Antenna GPS Receiver and Pitot Tube," *IEEE Transactions on Aerospace and Electronic Systems*, Vol. 47, No. 1, 2011, pp. 109–117.

[26] Johansen, T. A., Cristofaro, A., Sorensen, K. L., Hansen, J. M., and Fossen, T. I., "On Estimation of Wind velocity, Angle-of-attack and Sideslip Angle of Small UAVs using Standard Sensors," *2015 International Conference on Unmanned Aircraft Systems*, 2015, pp. 510–519.

[27] Wenz, A., Johansen, T. A., and Cristofaro, A., "Combining Model-free and Model-based Angle of Attack Estimation for Small Fixed-wing UAVs using a Standard Sensor Suite," *2016 International Conference on Unmanned Aircraft Systems*, 2016, pp. 624–632.

[28] Shawon, M. H., Chao, H., and Lin, Z., "Estimation of VerticalWind Velocity and Wake Parameters during UAS Wake Vortex Encounters," *AIAA SCITECH Forum*, 2024.

[29] Tian, P., Chao, H., Gu, Y., and Hagerott, S. G., "UAV Flight Test Evaluation of Fusion Algorithms for Estimation of Angle of Attack and Sideslip Angle," *AIAA Guidance, Navigation, and Control Conference*, 2016.

[30] Bishop, G., and Welch, G., "An Introduction to the Kalman Filter," *Proceedings of SIGGRAPH, Course*, Vol. 8, 2001, p. 41.

[31] Chao, H., Matt, J. J., Flanagan, H., Tian, P., and Gowravaram, S., "Atmospheric Sensing of Wildland Fire Plumes Using KHawk UAS," *20th Symposium on Meteorological Observation and Instrumentation*, 2020.

[32] "RiteWing Zephyr III Wing (Z3)," , 2024. URL `https://www.getfpv.com/ritewing-zephyr-iii-wing-z3.html`, accessed: 2024-11-12.

[33] Iowa State University Mesonet, "Weather Station, Kansas ASOS at Lawrence," , 2024. URL `https://mesonet.agron.iastate.edu/request/download.phtml?network=KS_ASOS`, accessed: 2024-11-08.

[34] Arreola Amaya, M., and Clements, C. B., "Evolution of Plume Core Structures and Turbulence during a Wildland Fire Experiment," *Atmosphere*, Vol. 11, No. 8, 2020.